

# Reversing the Resistivity Contrast in the Phase-Change Memory Material $\text{GeSb}_2\text{Te}_4$ Using High Pressure

HPSTAR  
2015-128

Ming Xu,\* Zhenhai Yu, Lin Wang, Riccardo Mazzarello, and Matthias Wuttig

Phase-change memory devices distinguish “1” and “0” states by the electrical contrast between the amorphous and the crystalline phases. Under ambient conditions, the amorphous phase normally exhibits a higher resistivity, exceeding its crystalline counterpart by 2–5 orders of magnitude. Here, however, it is demonstrated that such pronounced resistivity contrast is remarkably reduced and even reversed with increasing hydrostatic-like pressure in the prototypical phase-change material  $\text{GeSb}_2\text{Te}_4$  (GST). This anomalous resistivity reversal originates from the differences in the pressure-induced atomic rearrangement of these two phases, as revealed by *ab initio* molecular dynamics simulations. Specifically, a low to medium pressure (<7 GPa) primarily compresses the bonds in crystalline GST without significantly displacing the atoms and vacancies off the lattice sites. As a result, only relatively small changes in the band structure are induced. In contrast, in amorphous GST, the fraction of voids changes drastically with pressure and the Peierls-like distortion is greatly reduced, yet the average bond length remains almost constant. These effects eventually turn the semiconducting glass into a metallic one. Our work reveals distinct behaviors of amorphous and crystalline phase-change materials under stress, shedding light on the mechanisms of electronic transport in different phases, and thus may have important implications on the design of phase-change memory devices.

## 1. Introduction

Typical phase-change materials (PCMs), such as  $\text{GeSb}_2\text{Te}_4$  or  $\text{Ge}_2\text{Sb}_2\text{Te}_5$  (GST), are located on the tie-line between  $\text{GeTe}$  and  $\text{Sb}_2\text{Te}_3$  in the Ge–Sb–Te ternary phase diagram.<sup>[1]</sup> These chalcogenides share several common features, namely, fast and reversible switching between the amorphous and the crystalline phases, which is accompanied by large optical and electrical property contrasts, rendering their applications in data storage devices such as optical DVDs and electronic memories.<sup>[2]</sup> Over the past decade, there have been intense efforts to link these

unique features to the atomic structures, and by now many ingredients are well understood. For instance, crystalline GST (*c*-GST), one of the functional phases in memory devices, forms a rocksalt-like structure upon fast crystallization, with Te occupying one face-centered-cubic (fcc) sublattice and Ge/Sb/vacancies occupying the other.<sup>[3,4]</sup> The fraction of vacancies is determined by the stoichiometric difference between the atoms on the two sublattices, e.g.,  $\text{GeSb}_2\text{Te}_4$  has 25% vacancies on the Ge/Sb sublattice.<sup>[5]</sup> The stoichiometric vacancies ensure the three-*p*-valence-electron scenario and the peculiar resonant *p*-type bonding in *c*-GST.<sup>[6–8]</sup> Nevertheless, a small fraction of additional “excess” vacancies (0.1%–0.2%) is also present due to self-doping effects, yielding a large concentration of charge carriers. The random distribution of vacancies in the cation sites also affects the electrical properties because the resulting disorder can lead to Anderson localization of electrons.<sup>[9–12]</sup> On the other hand, amorphous GST (*a*-GST) has been pictured to contain mainly right-

angle *p*-type bonds (with a small fraction of tetrahedrally coordinated Ge) and a large amount of vacant areas (or voids) that pervade the whole lattice.<sup>[13–16]</sup> The local defective octahedral motifs and the free volumes between them are supposed to play an important role in the fast crystallization upon heating.<sup>[17–20]</sup>

Although present memory devices are mostly driven by heat, applying other thermodynamic parameters such as pressure (*P*) has opened new dimensions to probe the structure–property relation in PCMs.<sup>[21–29]</sup> Interesting *P*-induced phase transformations have been reported for GST, showing that both *a*-GST and *c*-GST turn into high-density amorphous phases,

Dr. M. Xu, Prof. M. Wuttig  
I. Institute of Physics (IA)  
RWTH Aachen University  
Aachen 52074, Germany  
E-mail: xu@physik.rwth-aachen.de  
Dr. Z. Yu, Prof. L. Wang  
Center for High Pressure  
Science and Technology Advanced  
Research (HPSTAR)  
Shanghai 201203, China

DOI: 10.1002/aelm.201500240

Prof. L. Wang  
High Pressure Synergetic Consortium (HPSynC)  
Carnegie Institution of Washington  
Argonne, IL 60439, USA  
Prof. R. Mazzarello  
Institute for Theoretical Solid State Physics  
RWTH Aachen University  
Aachen 52074, Germany  
Prof. R. Mazzarello, Prof. M. Wuttig  
JARA-FIT and JARA-HPC  
RWTH Aachen University  
Aachen 52056, Germany



which resemble each other at around 15 GPa,<sup>[25]</sup> and such amorphous phases persist upon decompression to ambient  $P$ . Resistivity measurements performed on  $a$ -GST<sup>[30]</sup> have shown that the conductivity of this semiconducting glass increases by four orders of magnitude at high  $P$  and such property change is reversible upon decompression. Ab initio molecular dynamics (AIMD) simulations have discovered strong correlations between the resistivity and voids in  $a$ -GST.<sup>[30]</sup>

In this work, we have performed high- $P$  resistivity measurements on  $c$ -GST. We compressed  $c$ -GST up to  $\approx 20$  GPa and then slowly released the pressure. Meanwhile, the electrical resistivity ( $\rho$ ) was measured in situ by the four-point method. The resistivity drops by two orders of magnitude before  $c$ -GST transforms to  $a$ -GST. Upon decompression, the resistivity of the amorphous product remains metallic down to 7 GPa (15–7 GPa) but increases drastically by more than four orders of magnitude in the low- $P$  regime (7–0 GPa). Interestingly,  $a$ -GST is more conductive than  $c$ -GST in the range of 3–15 GPa, opposite to the behavior at ambient  $P$ . AIMD simulations reveal that a medium  $P$  ( $\approx 7$  GPa) is able to tune the bandgap in  $a$ -GST by compressing voids and reducing the Peierls-like distortion without changing the average bond length. This is opposite to the  $c$ -GST case, in which the bonds are shortened while the lattice distortion does not increase considerably. The understanding of atomic and electronic behaviors of PCMs under pressure is important for memory devices, which work under fairly high stresses due to the mismatch of crystalline and amorphous densities.<sup>[31]</sup> Moreover, our work offers a new method to engineer the band structure by tuning the voids and the local distortion with  $P$ , paving the way for the development of novel devices that are driven by elastic strains or even hydrostatic pressures.<sup>[32]</sup>

## 2. Experimental Results

The four-point resistivity measurement was carried out on  $c$ -GST in a diamond anvil cell (DAC), which is depicted in Figure 1a (detailed descriptions of the experiments are illustrated in Experimental Section) and the results are plotted in Figure 1b. The  $c$ -GST film was annealed at 175 °C with an initial sheet resistivity of  $\approx 0.1 \Omega \text{ cm}$ . We then peeled off the film and filled the steel holder with these  $c$ -GST powders. The sample was pressed to  $\approx 2$  GPa to ensure good contact and was then subject to the elevating  $P$ . From 2 to 15 GPa, the resistivity drops from 0.05 to 0.002  $\Omega \text{ cm}$ , approximately by one order of magnitude. We further increased  $P$  to  $\approx 20$  GPa to ensure that  $c$ -GST is fully amorphized (previous synchrotron diffraction experiments showed that  $c$ -GST becomes amorphous at  $\approx 15$  GPa.<sup>[21,22]</sup> This transition is subsequently confirmed by our AIMD simulations in the following section). Above 15 GPa, the resistivity saturates around 0.001  $\Omega \text{ cm}$ . The blue dashed line in Figure 1b marks the critical resistivity ( $\approx 0.002 \Omega \text{ cm}$ ) where the insulator–metal transition takes place in  $c$ -GST by reducing the vacancy disorder at ambient  $P$ .<sup>[9]</sup> This critical value is consistent with Mott's minimum metallic conductivity (above which the material behaves like a metal).<sup>[33,34]</sup> Notice that, in  $c$ -GST, the metallic behavior in the low-disorder limit (at ambient  $P$ ) stems from the p-doping due to the excess vacancies.<sup>[9,10]</sup> It is reasonable to assume that

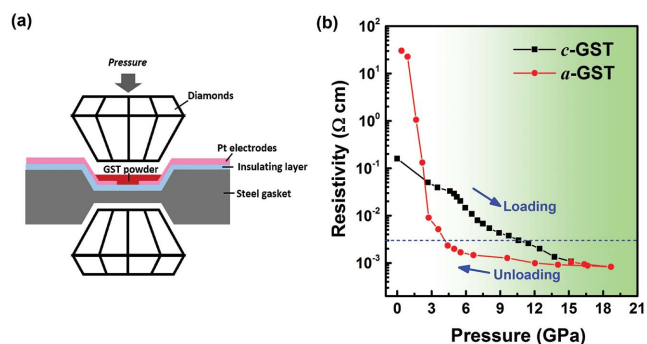


**Figure 1.** The experimental setup and the results of the high  $P$  resistivity measurement. a) The schematic diagram of the experimental setup for high  $P$  resistivity measurements. b) The resistivity of GST sample upon compression and decompression.  $c$ -GST can survive the high  $P$  of  $\approx 15$  GPa before fully transformed into the metallic-like  $a$ -GST. The resistivity of  $c$ -GST slowly decreases (almost linearly) with  $P$  by  $\approx 2$  orders of magnitude. Upon decompression, the amorphous phase is retained and its resistivity first remains metallic and then increases precipitously when the  $P$  approaches zero.  $a$ -GST has higher resistivity than  $c$ -GST at 0–3 GPa, but the resistivity contrast is reversed at higher  $P$  (3–15 GPa). The blue dash line in (b) qualitatively separates the metal and the insulator, according to the insulator–metal transition in  $c$ -GST<sup>[9]</sup> and Mott's minimum metallic conductivity.<sup>[34]</sup>

Mott's criterion may hold true in similar  $\text{GeSb}_2\text{Te}_4$  references, thus the  $P$ -amorphized GST above 7 GPa may be qualitatively described as a high-density and metallic-like glass.

Interestingly, the resistivity does not bounce back immediately when  $P$  is slowly removed. The amorphous phase remains metallic-like until  $P$  is reduced to  $\approx 7$  GPa. This metallic-like resistivity of  $a$ -GST (15–7 GPa) is stable and does not vary significantly upon relaxation of the sample. Below 7 GPa, however, the resistivity of  $a$ -GST starts to increase drastically upon decompression, and matches with that of  $c$ -GST at  $\approx 3$  GPa. As shown in Figure 1b,  $a$ -GST is even more conductive than  $c$ -GST in the range between 3 and 15 GPa. This appears to be counter-intuitive because phase-change memory devices are mainly based on the resistivity switching between high-resistive  $a$ -GST and low-resistive  $c$ -GST under ambient conditions.

The hysteresis loop that appears in Figure 1b is partially due to slow kinetics: the relaxation of the  $P$ -amorphized  $a$ -GST requires much longer time than our observation period. However, the fact that  $P$  also reverses the resistivity between the loading disordered  $c$ -GST and the loading as-deposited  $a$ -GST<sup>[30]</sup> (Figure S2, Supporting Information) confirms that the resistivity reversal between  $a$ -GST and  $c$ -GST is independent of the amorphous phase we choose. Such distinct changes of the resistivity in  $a$ -GST and  $c$ -GST with pressure (i.e., the fact that the resistivity of  $a$ -GST drops much faster than that of  $c$ -GST upon compression, as shown in Figure 1b) hints at different mechanisms of atomic rearrangement in these two phases. To this end, we have performed AIMD simulations to trace the origin of this resistivity reversal under pressure.

## 3. AIMD Results and Discussions

AIMD simulations were performed to mimic the entire loading and unloading process up to  $\approx 20$  GPa (details are described in

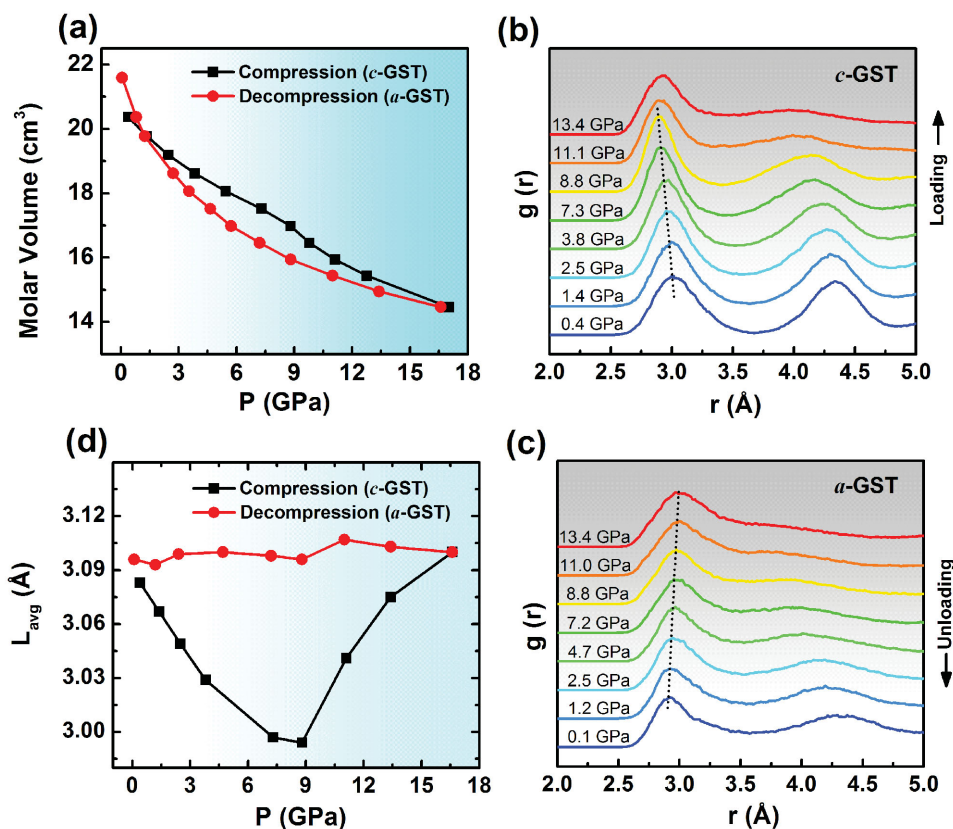


**Figure 2.** Mass density and bond changes of GST with  $P$  revealed by AIMD simulations. a) The equation of states (pressure-volume relation) of GST under  $P$ .  $a$ -GST has lower density than  $c$ -GST at the ambient pressure, but a low  $P$  ( $\approx 2$  GPa) can reverse it. b,c) The pair distribution functions (PDFs) of  $c$ -GST and  $a$ -GST under various pressures. The first peak of the PDFs of  $c$ -GST shifts to the left with increasing  $P$  (0–9 GPa) but that of  $a$ -GST skews to the opposite direction. d) The average bond lengths as a function of  $P$ . The bonds of  $c$ -GST are compressed by 3% at 0–7 GPa and then start to recover when  $P > 9$  GPa due to the atomic distortion in releasing the strain energy. The average bond length of  $a$ -GST, however, remains almost invariant in the entire  $P$  range.

Experimental Section). Although DFT yields 2%–3% larger lattice parameters and bond lengths than the experimental data for both polymorphs,<sup>[35,36]</sup> the trend of the mass density changes can still be unambiguously identified. Equations of states (EOS) for  $c$ -GST and  $a$ -GST are plotted in **Figure 2a**, clearly showing that the volume of  $a$ -GST reduces faster than  $c$ -GST with increasing  $P$  and the glass becomes denser than its crystalline counterpart within 3–15 GPa. The compression and decompression of the single-phase  $a$ -GST and  $c$ -GST (without phase transformations) both show very small hysteresis loops, but the gap between these two phases are obviously larger, emphasizing on the salient structural difference between  $a$ -GST and  $c$ -GST (Figure S3, Supporting Information). The density change coincides with the concomitant resistivity reversal (Figure 1b), as discussed in the previous section, indicating strong correlations between them. In principle, the increase of density can be attributed to different factors, including the compression of interatomic distances<sup>[27,37]</sup> (e.g., the shortening of the bonds without changing the symmetry or local order of the lattice), the compression of vacant regions (which are present in most chalcogenides<sup>[30]</sup>), or the rearrangement of local atomic clusters (such as close-packed metallic glasses containing few free volumes<sup>[37]</sup>). The key to understanding why  $a$ -GST is more compressible than  $c$ -GST under high  $P$  is to distinguish which mechanism dominates at a given  $P$ .

To this end, we calculated the pair distribution functions (PDFs),  $g(r)$ , of  $c$ -GST (loading) and  $a$ -GST (unloading) in **Figure 2b,c**. The position of the first peak of the PDF has been conventionally utilized to determine the bond length. In **Figure 2b**, the first peak of the PDF of  $c$ -GST shifts to the left (towards shorter  $r$ ) upon compression, indicating that the bonds are indeed shortened, which is expected owing to the volume reduction of the simulation boxes. Surprisingly, the PDF peaks of  $a$ -GST skew to the opposite direction with increasing  $P$ , similar to the “negative expansion” phenomenon occurring in some supercooled metallic liquids, which exhibit an anomalous shift of the PDF peaks towards shorter  $r$  upon increasing temperature.<sup>[38,39]</sup> Ding et al.<sup>[40]</sup> argued that such anomalous shift does not necessarily link to a change in the average bond length because it can stem from the asymmetry in the PDF peak profile (i.e., the area of the left part of PDF peak is smaller than the right part in **Figure 2c**). Therefore, one should study the entire first-peak profile to evaluate the bond length. In this sense, we calculated the average bond length ( $L_{\text{avg}}$ ) by the following equation:

$$L_{\text{avg}} = \frac{\int_0^{r_{\text{max}}} r \cdot 4\pi r^2 g(r) dr}{\int_0^{r_{\text{max}}} 4\pi r^2 g(r) dr} \quad (1)$$

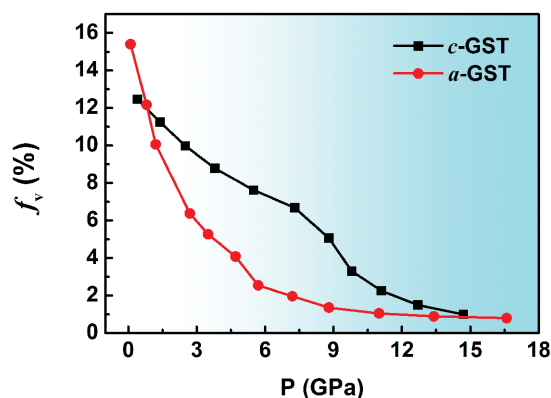


**Figure 3.** The fraction ( $f_v$ ) of vacancies in *c*-GST and voids in *a*-GST under high  $P$ . The vacancies and voids are identified with the low-electron-density regions.<sup>[30]</sup> The criterion to separate the low- and high-electron-density regions is determined by *c*-GST, which contains 12.5% vacant areas under ambient  $P$ . The visualizations of vacancies/voids in GST are displayed in Figure S4, Supporting Information.

where  $r_{\max}$  is the location of the first minimum of a PDF profile. The change of  $L_{\text{avg}}$  against pressure is plotted in Figure 2d. The  $L_{\text{avg}}$  of *c*-GST is shortened at 0–9 GPa, as expected from Figure 2b. But interestingly, the bond length is elongated above  $\approx 9$  GPa. This is because high  $P$  ( $>9$  GPa) severely distorts the lattice by shifting atoms to the neighboring vacancy sites to release the strain energy, triggering the collapse of *c*-GST into *a*-GST.<sup>[21,22]</sup> On the contrary, *a*-GST behaves differently from *c*-GST under  $P$ : the  $L_{\text{avg}}$  in this glass is almost unchanged.

More quantitatively, the lattice parameter of *c*-GST is compressed by  $\approx 7\%$  at about 9 GPa but the bond length is shortened by  $\approx 3\%$ , while the lattice parameter of *a*-GST is reduced by 11% but the bond length changes by less than 1%. Apparently, the minor change of bond length is not the reason of the large density change under  $P$  and a more important factor should be responsible. Intuitively, the large amount of intrinsic vacancies in *c*-GST or corresponding voids in *a*-GST should account for this change.<sup>[30]</sup> To map out the vacancies/voids of random shapes and sizes in the GST models, we calculated the density of electrons and identified vacancies/voids by “vacant areas” in which electrons are sparsely distributed. Such low-electron-density regions indicate the absence of strong covalent bonds, which involves sharing of electrons. A cutoff of electron density  $\rho_e(r)$  that separates the low- and the high-electron-density regions can be determined from crystalline  $\text{GeSb}_2\text{Te}_4$  at ambient  $P$ , where the fraction of low-electron-density regions ought to be 12.5%. The cutoff has been scaled with the box size, in that  $P$  reduces the volume of the supercell and increases the average electron density.

**Figure 3** shows the change of the fraction of vacancies/voids ( $f_v$ ) during the compression and decompression process. *c*-GST initially contains 12.5% vacancies at ambient  $P$ . The fraction of vacant areas gradually shrinks at low-to-medium pressures (0–7 GPa) owing to slight distortions around vacancies. Nevertheless, the position of atoms and vacancies remains largely unchanged (Figure S4, Supporting Information). At higher  $P$ , however, the vacancies in *c*-GST start to be squeezed out when nearby atoms displace towards the neighboring

vacancies to release the strong strain energy from the bond compression.<sup>[22]</sup> Such atomic rearrangement is in line with the bond length elongation in *c*-GST above 9 GPa (Figure 2d). On the other hand, *a*-GST contains  $\approx 4\%$  more vacant regions than *c*-GST at the low- $P$  end, but these voids are pressed out much faster than the vacancies in *c*-GST are. At  $\approx 7$  GPa, *a*-GST even has 5% less vacant regions than *c*-GST (visualized in Figure S4, Supporting Information). Hence, the basic reason why the density of *a*-GST changes rapidly is that the voids are much easier to compress than the covalent bonds. This conclusion agrees with the previous experimental study showing that, although *a*-GST has stiffer bonds than *c*-GST, its bulk modulus is significant lower.<sup>[41–43]</sup>

To further rationalize the atomic arrangements and link them to the electronic properties in GST, we analyzed the Peierls-like distortion (PD), which refers to the displacement of a sublattice away from the “central position” in order to lower the electronic energy, giving rise to collinear short-long bond pairs and entailing the opening of the bandgap.<sup>[44–46]</sup> Most crystalline chalcogenides contain some degrees of PD, and pairs of collinear short-long bonds indicative of PD occur in liquid and amorphous PCMs as well.<sup>[47,48]</sup> In general, the stronger the PD is, the larger the bandgap is expected to be.<sup>[48]</sup> In **Figure 4**, we plot the length distributions of near-collinear bonds (bond angles are chosen between  $160^\circ$  and  $180^\circ$  and the distance cutoff is 4.6 Å). Figure 4a shows that PD in *c*-GST is not as prominent as in crystalline GeTe: its near-collinear short/long bonds are distributed around 2.93/3.10 Å (Figure 4a), compared with crystalline GeTe whose short/long bonds are 2.85/3.28 Å.<sup>[49,50]</sup> Moreover the change of the PD in *c*-GST with  $P$  appears to be subtle, e.g., a medium  $P$  ( $\approx 7$  GPa) compresses the lattice uniformly and shortens both short and long bonds into 2.88/3.00 Å (Figure 4b). In contrast, at ambient  $P$ , PD is very pronounced in *a*-GST: the short bonds are distributed around 2.90 Å, while the “long bonds” are peaked at 3.28 Å and can extend to 4.50 Å (Figure 4c). The tail in the bond distribution is a result of the large distance cutoff employed (4.6 Å), such that atoms separated by voids are all considered. The tail does not contribute to the average bond lengths in Figure 2d, which were obtained by considering only the bonds below the first minimum of the PDFs (corresponding to 3.3–3.5 Å). Above 7 GPa, the “long bonds” (particularly the tail above 3.3–3.5 Å) that are separated by voids are compressed sharply into 3.07 Å and hence the PD of *a*-GST is largely suppressed (Figure 4d). This finding demonstrates that  $P$  significantly changes the PD of the void-ridden amorphous state and hence may have strong effects on its electronic properties.

So far we have shown strong concurrence between the resistivity and the vacancy/void concentration in *a*-GST and *c*-GST, both exhibiting a reversal under  $P$ . To establish the physical correlation between the structure and the property, one needs to take into account the unique mechanisms of electron transport in both phases. At ambient  $P$ , the large carrier concentration and large conductivity of *c*-GST originate from the presence of excess non-stoichiometric Ge/Sb/vacancies, which turn the system into a p-type semiconductor.<sup>[2]</sup> Remarkably, in *a*-GST such defects do not lead to a shift of the Fermi level, which remains pinned at the center of the bandgap.<sup>[51]</sup> This different behavior leads to the electronic contrast between crystalline and amorphous GST. It has been suggested that the pinning

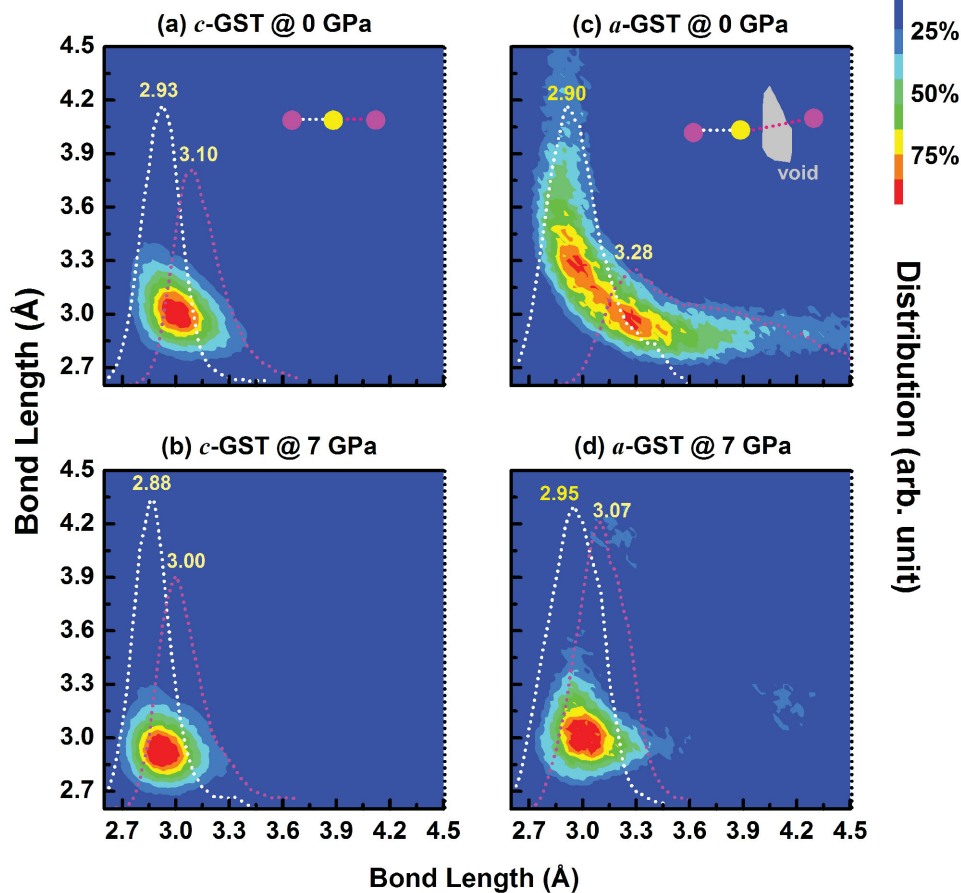


**Figure 4.** Distributions of near-collinear bond lengths. In addition to the contour maps, the distribution of near-collinear short bonds (white dot lines) and long bonds (pink dot lines) is plotted separately as well. The peak values of the bond length distribution are marked (in Å). As seen in a,b), although the PD is an intrinsic property in many crystalline chalcogenides, it seems not as prominent in *c*-GST as in GeTe. A medium *P* (7 GPa) compresses the lattice uniformly and all the bonds are shortened isotropically, thus the change of PD is relatively small. In contrast, as shown in c,d), the PD is very evident in *a*-GST at ambient *P*, but it is significantly reduced at 7 GPa, probably due to the removal of voids.

of the Fermi energy in *a*-GST is a consequence of the flexibility of the amorphous network, which enables it to absorb excess electrons/holes from the defects (e.g., via valence alternation or polyvalency<sup>[13,14]</sup>) and remain insulating.<sup>[5]</sup>

The amorphous phase is intrinsically disordered due to the random distribution of atoms.<sup>[51]</sup> In such disordered materials, the movement of electrons is governed by the trap-limited electronic transport<sup>[52]</sup> (the electrons occupying extended states are responsible for this transport but they are occasionally trapped by the localized states nearby) and variable range hopping<sup>[53]</sup> (electrons carry current by hopping between localized states near the Fermi level). According to the distinct temperature dependences of these two mechanisms, previous experiments found that the trap-limited mechanism (governed by extended electrons) is responsible for the electron transport in *a*-GST at room temperature.<sup>[54]</sup> Because of this, even a small change of the bandgap increases the carrier concentration significantly and has pronounced influence on the electrical conductivity. When the voids in *a*-GST are squeezed out, the interaction between atomic clusters, which are strongly affected by *P*,<sup>[30]</sup> becomes enhanced and hence the PD is reduced, leading to the shrinkage or even closure of the bandgap,<sup>[55]</sup> as shown in **Figure 5**.

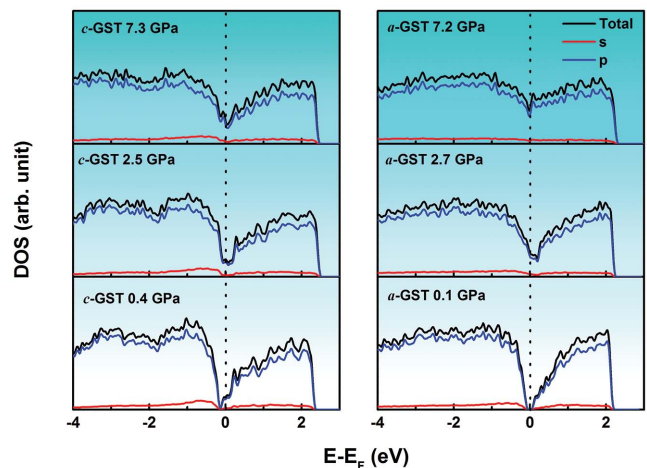


**Figure 5.** Density of states (DOS) of *c*-GST and *a*-GST under various pressures. At ambient *P*, *a*-GST normally has slightly larger bandgap than *c*-GST. But due to the rapid reduction of PD upon compression, the bandgap of *a*-GST reduces faster than that of *c*-GST. At  $\approx 7$  GPa, the bandgap of *a*-GST almost vanishes while *c*-GST still shows a ditch.

*c*-GST also exhibits complex electron transport due to the random distribution of vacancies on the cation sites. Such disorder gives rise to localized states near the valence band and insulating behavior at very low temperature.<sup>[10,56]</sup> Different annealing temperatures can tune the disorder, significantly changing the mobility of the charge carriers, but the concentration of them is barely altered.<sup>[9]</sup> Figure 5 indicates that, although *P* is able to decrease the bandgap of *c*-GST (and, thus, increase the concentration of charge carriers), the reduction is not as fast as that of *a*-GST and a gap-like ditch is present even at  $\approx 7$  GPa. This is because only moderate decrease in PD occurs, and the slight bond compression has minor influence on the bandgap. The less-pronounced change of the band structure of *c*-GST is the main reason that the resistivity of *c*-GST drops more slowly than *a*-GST under *P*, leading to the resistivity reversal.

Our work has important implications on PCM devices. For example, previous study demonstrated that the volume of GST expanded by  $\approx 7\%$  when it transformed from a crystal to a glass by heating,<sup>[31]</sup> indicating that *a*-GST is inevitably subjected to pressure (or stress) when it is confined by the surrounding *c*-GST matrix in a PCM memory cell. Such pressure is not high enough to reverse the resistivity, but could significantly reduce the resistivity contrast between *a*-GST and *c*-GST and may lead to the failure of data reading (the electronic memory devices read data by distinguishing the resistivity contrast between “1” and “0” states). Our study advises the memory devices to be designed with less confinement to dissipate the stress during the phase transition. Furthermore, the tuning of the resistivity by pressure opens a new window of opportunity for multi-state memory devices driven by elastic strains or even hydrostatic pressures.<sup>[32]</sup>

#### 4. Conclusions

We have measured the resistivity of the phase-change material GST under high *P*. *c*-GST is compressed to  $\approx 20$  GPa and becomes amorphous irreversibly. Interestingly, the resulting amorphous phase has a lower resistivity than *c*-GST at 3–15 GPa, opposite to the behavior at ambient *P*. AIMD simulations reveal that the low to medium *P* ( $< 7$  GPa) slightly compresses the bonds of *c*-GST but leave the average bond length in *a*-GST mostly unaffected. However, the fraction of voids in *a*-GST is decreased dramatically, while the vacancies in *c*-GST are largely retained. The bandgap of *a*-GST is almost closed up at  $\approx 7$  GPa because the compression of voids reduces the Peierls-like distortion, resulting in the overlap of the conduction and the valence bands. In contrast, the gap of *c*-GST appears not to be entirely vanished under medium *P*, consistent with the insignificant change in the crystalline lattice and the Peierls-like distortion. The understanding of pressure-induced atomic behaviors of amorphous and crystalline phases in this work is important in the control of electronic properties in PCMs and has implications on the design of memory devices to reduce the stress in the PCM cells.

#### 5. Experimental Section

**High *P* Resistivity Measurement:** GST films were sputtered on the glass substrates and annealed at 175 °C for 30 min. The rocksalt structure of *c*-GST was then confirmed by the X-ray diffraction (Figure S1, Supporting Information) and the powders from this film were later

used for the resistivity measurement under high pressure. A dent was pressed on a stainless steel sheet by diamond anvil cell (DAC) and an insulating BN layer was coated on the sheet. Four Pt foil electrodes were fixed above the BN layer and the dent was then filled by GST powders (Figure 1a). The sample was pre-hardened to 2–3 GPa to ensure good contact. The GST powders are expected to act as a pressure transmitting medium themselves to generate hydrostatic-like pressures due to the good malleability of this material. The values of *P* were determined by the fluorescence of a ruby, which was embedded in the GST powder.<sup>[57]</sup>

High *P* was then applied to *c*-GST powders in steps of 1–2 GPa up to 20 GPa, at which *c*-GST was fully transformed to the amorphous phase. Afterward we slowly released *P* in the same pace. An electrical current of 0.5–1.0 mA was injected into the electrodes and two sets of resistance values ( $R_1$  and  $R_2$ ) were recorded for each *P* step by switching the electrodes. Such electrical current entails small current density, which does not lead to the phase transition of the sample. The resistivity  $\rho$  can be calculated by solving the equation  $\exp(-\pi t R_1 / \rho) + \exp(-\pi t R_2 / \rho) = 1$ . The initial thickness of *c*-GST sample *t* was estimated to be 10  $\mu\text{m}$  and we changed the *t* values, varying between 7.0 and 11.0  $\mu\text{m}$ , under different pressures according to the equation of states in Figure 2a. We recorded the resistivity data at least 30 min after each compression (decompression) itinerary to ensure that the sample was mostly relaxed and the change of the resistivity data slowed down.

The GST films were fabricated and analyzed at I. Institute of physics in RWTH Aachen University, Germany. High *P* experiments were carried out at the High Pressure Synergetic Consortium (HPSynC), Advanced Photon Source, Argonne National Laboratory in Chicago and the Center for High Pressure Science and Technology Advanced Research (HPSTAR) in Shanghai.

**AIMD Simulations:** The density functional theory (DFT) simulations were performed using the projector augmented-wave (PAW) method with the generalized gradient approximation (GGA), by the Vienna ab initio simulation package (VASP) code.<sup>[58–60]</sup> A supercell with 189 atoms of *c*-GeSb<sub>2</sub>Te<sub>4</sub> was first relaxed at 0 K to zero pressure (the DFT-derived lattice parameters, either *c*-GST or *a*-GST, are 2%–3% larger than the experimental data,<sup>[61]</sup> as seen in Figure 2a). The lattice parameter of the box was then reduced isotopically by 1% and AIMD simulations were performed on this model at 300 K for 12 ps. The volume reduction was repeated to mimic the hydrostatic-like compression in experiments and the AIMD simulations allowed models to relax for 12 ps every step so that the energy fluctuation became relatively small. The decompression process was started after the pressure reached  $\approx 20$  GPa. Likewise, the lattice parameter was increased in steps of 1% and 12 ps of AIMD simulations were run for each step until the pressure was approximated to zero.

Different box sizes (with 84, 189, 448, and 1008<sup>[12]</sup> atoms) were also tested in our simulations to minimize the size effects. Small boxes with 84 atoms or less recrystallize easily at 300 K upon decompression, inconsistent with experimental observations. Instead, the physical properties and the transition behavior of the 189-atom boxes are very similar to the 448-atom and the 1008-atom ones, in terms of coordination number, the bond length, and most importantly, the transition pressure (all occur at 13–15 GPa). Thus, a supercell with 189 atoms exhibits reasonable consistency and efficiency in simulating the high *P* behavior of GST materials.

#### Supporting Information

Supporting Information is available from the Wiley Online Library or from the author.

#### Acknowledgements

The authors are indebted to Wei Zhang for useful discussions. The research leading to these results had received funding from the European Union Seventh Framework Programme (FP7/2007–2013) under Grant

Agreement No. 340698 (ERC Advanced Grant "Disorder Control"). Computational resources are granted by JARA-HPC under the project of JARA0114. M.X. acknowledges Alexander von Humboldt Foundation and RWTH Start-Up Program (funded by the Excellence Initiative of the German federal and state governments). L.W. acknowledges Natural Science Foundation of China (Grant No. 11004072) and the Program for New Century Excellent Talents in University (NCET-10-0444). Z.Y. and L.W. acknowledge the support of NSAF (Grant No. U1530402). R.M. and M.W. acknowledge Deutsche Forschungsgemeinschaft (SFB 917 Nanoswitches).

Received: July 30, 2015

Revised: September 13, 2015

Published online: October 27, 2015

- [1] M. Wuttig, N. Yamada, *Nat. Mater.* **2007**, *6*, 824.
- [2] D. Lencer, M. Salinga, M. Wuttig, *Adv. Mater.* **2011**, *23*, 2030.
- [3] N. Yamada, T. Matsunaga, *J. Appl. Phys.* **2000**, *88*, 7020.
- [4] X. Q. Liu, X. B. Li, L. Zhang, Y. Q. Cheng, Z. G. Yan, M. Xu, X. D. Han, S. B. Zhang, Z. Zhang, E. Ma, *Phys. Rev. Lett.* **2011**, *106*, 025501.
- [5] S. Caravati, M. Bernasconi, T. D. Kuhne, M. Krack, M. Parrinello, *J. Phys.-Condens. Matter* **2009**, *21*, 255501.
- [6] M. Wuttig, D. Lusebrink, D. Wamwangi, W. Welnic, M. Gillissen, R. Dronskowski, *Nat. Mater.* **2007**, *6*, 122.
- [7] M. Wuttig, *Phys. Status Solidi B* **2009**, *246*, 1820.
- [8] K. Shportko, S. Kremers, M. Woda, D. Lencer, J. Robertson, M. Wuttig, *Nat. Mater.* **2008**, *7*, 653.
- [9] T. Siegrist, P. Jost, H. Volker, M. Woda, P. Merkelbach, C. Schlockermann, M. Wuttig, *Nat. Mater.* **2011**, *10*, 202.
- [10] W. Zhang, A. Thiess, P. Zalden, R. Zeller, P. H. Dederichs, J. Y. Raty, M. Wuttig, S. Blugel, R. Mazzarello, *Nat. Mater.* **2012**, *11*, 952.
- [11] P. W. Anderson, *Phys. Rev.* **1958**, *109*, 1492.
- [12] M. Xu, W. Zhang, R. Mazzarello, M. Wuttig, *Adv. Sci.* **2015**, *2*, 1500117.
- [13] M. Xu, Y. Q. Cheng, H. W. Sheng, E. Ma, *Phys. Rev. Lett.* **2009**, *103*, 195502.
- [14] M. Krbal, A. V. Kolobov, P. Fons, J. Tominaga, S. R. Elliott, J. Hegedus, T. Uruga, *Phys. Rev. B* **2011**, *83*, 054203.
- [15] J. Akola, J. Larrucea, R. O. Jones, *Phys. Rev. B* **2011**, *83*, 094113.
- [16] V. L. Deringer, W. Zhang, M. Lumeij, S. Maintz, M. Wuttig, R. Mazzarello, R. Dronskowski, *Angew. Chem. Int. Ed.* **2014**, *53*, 10817.
- [17] D. Loke, T. H. Lee, W. J. Wang, L. P. Shi, R. Zhao, Y. C. Yeo, T. C. Chong, S. R. Elliott, *Science* **2012**, *336*, 1566.
- [18] J. Orava, A. L. Greer, B. Gholipour, D. W. Hewak, C. E. Smith, *Nat. Mater.* **2012**, *11*, 279.
- [19] M. Salinga, E. Carria, A. Kaldenbach, M. Bornhofft, J. Benke, J. Mayer, M. Wuttig, *Nat. Commun.* **2013**, *4*, 2371.
- [20] I. Ronneberger, W. Zhang, H. Eshet, R. Mazzarello, *Adv. Funct. Mater.* **2015**, DOI: 10.1002/adfm.201500849.
- [21] A. V. Kolobov, J. Haines, A. Pradel, M. Ribes, P. Fons, J. Tominaga, C. Steimer, G. Aquilanti, S. Pascarelli, *Appl. Phys. Lett.* **2007**, *91*, 021911.
- [22] S. Caravati, M. Bernasconi, T. D. Kuhne, M. Krack, M. Parrinello, *Phys. Rev. Lett.* **2009**, *102*, 205502.
- [23] M. Krbal, A. V. Kolobov, P. Fons, J. Haines, A. Pradel, M. Ribes, A. A. Piarristeguy, C. Levelut, R. Le Parc, V. Agafonov, M. Hanfland, J. Tominaga, *Phys. Rev. B* **2011**, *83*, 024105.
- [24] Y. Q. Cheng, M. Xu, H. W. Sheng, Y. Meng, X. D. Han, E. Ma, *Appl. Phys. Lett.* **2009**, *95*, 131904.
- [25] M. Xu, Y. Meng, Y. Q. Cheng, H. W. Sheng, X. D. Han, E. Ma, *J. Appl. Phys.* **2010**, *108*, 083519.
- [26] B. Kalkan, S. Sen, J.-Y. Cho, Y.-C. Joo, S. M. Clark, *Appl. Phys. Lett.* **2012**, *101*, 151906.
- [27] Z. M. Sun, J. Zhou, Y. C. Pan, Z. T. Song, H. K. Mao, R. Ahuja, *Proc. Natl. Acad. Sci. USA* **2011**, *108*, 10410.
- [28] M. Krbal, A. V. Kolobov, J. Haines, P. Fons, C. Levelut, R. Le Parc, M. Hanfland, J. Tominaga, A. Pradel, M. Ribes, *Phys. Rev. Lett.* **2009**, *103*, 115502.
- [29] M. Krbal, A. V. Kolobov, J. Haines, A. Pradel, M. Ribes, P. Fons, J. Tominaga, C. Levelut, R. Le Parc, M. Hanfland, *Appl. Phys. Lett.* **2008**, *93*, 031918.
- [30] M. Xu, Y. Q. Cheng, L. Wang, H. W. Sheng, Y. Meng, W. G. Yang, X. D. Han, E. Ma, *Proc. Natl. Acad. Sci. USA* **2012**, *109*, E1055.
- [31] T. P. L. Pedersen, J. Kalb, W. K. Njoroge, D. Wamwangi, M. Wuttig, F. Spaepen, *Appl. Phys. Lett.* **2001**, *79*, 3597.
- [32] J. Li, Z. W. Shan, E. Ma, *MRS Bull.* **2014**, *39*, 108.
- [33] N. F. Mott, *Adv. Phys.* **1967**, *16*, 49.
- [34] N. F. Mott, *Int. Rev. Phys. Chem.* **1985**, *4*, 1.
- [35] J. Hegedus, S. R. Elliott, *Nat. Mater.* **2008**, *7*, 399.
- [36] J. Akola, R. O. Jones, S. Kohara, S. Kimura, K. Kobayashi, M. Takata, T. Matsunaga, R. Kojima, N. Yamada, *Phys. Rev. B* **2009**, *80*, 020201.
- [37] H. W. Sheng, H. Z. Liu, Y. Q. Cheng, J. Wen, P. L. Lee, W. K. Luo, S. D. Shastri, E. Ma, *Nat. Mater.* **2007**, *6*, 192.
- [38] H. B. Lou, X. D. Wang, Q. P. Cao, D. X. Zhang, J. Zhang, T. D. Hu, H. K. Mao, J. Z. Jiang, *Proc. Natl. Acad. Sci. USA* **2013**, *110*, 10068.
- [39] G. W. Lee, A. K. Gangopadhyay, K. F. Kelton, R. W. Hyers, T. J. Rathz, J. R. Rogers, D. S. Robinson, *Phys. Rev. Lett.* **2004**, *93*, 037802.
- [40] J. Ding, M. Xu, P. F. Guan, S. W. Deng, Y. Q. Cheng, E. Ma, *J. Chem. Phys.* **2014**, *140*, 064501.
- [41] T. Matsunaga, N. Yamada, R. Kojima, S. Shamoto, M. Sato, H. Tanida, T. Uruga, S. Kohara, M. Takata, P. Zalden, G. Bruns, I. Sergueev, H. C. Wille, R. P. Hermann, M. Wuttig, *Adv. Funct. Mater.* **2011**, *21*, 2232.
- [42] J. Kalb, F. Spaepen, T. P. Leervad Pedersen, M. Wuttig, *J. Appl. Phys.* **2003**, *94*, 4908.
- [43] T. Blachowicz, M. G. Beghi, G. Güntherodt, B. Beschoten, H. Dieker, M. Wuttig, *J. Appl. Phys.* **2007**, *102*, 093519.
- [44] J. P. Gaspard, F. Marinelli, A. Pellegatti, *EPL (Europhys. Lett.)* **1987**, *3*, 1095.
- [45] J. P. Gaspard, A. Pellegatti, F. Marinelli, C. Bichara, *Philos. Mag. Part B* **1998**, *77*, 727.
- [46] Z. M. Sun, J. Zhou, H. K. Mao, R. Ahuja, *Proc. Natl. Acad. Sci. USA* **2012**, *109*, 5948.
- [47] J. Y. Raty, V. Godlevsky, P. Ghosez, C. Bichara, J. P. Gaspard, J. R. Chelikowsky, *Phys. Rev. Lett.* **2000**, *85*, 1950.
- [48] J. Y. Raty, W. Zhang, J. Luckas, C. Chen, R. Mazzarello, C. Bichara, M. Wuttig, *Nat. Commun.* **2015**, *6*, 7567.
- [49] V. L. Deringer, M. Lumeij, R. P. Stoffel, R. Dronskowski, *Chem. Mater.* **2013**, *25*, 2220.
- [50] D. Lencer, M. Salinga, B. Grabowski, T. Hickel, J. Neugebauer, M. Wuttig, *Nat. Mater.* **2008**, *7*, 972.
- [51] R. Zallen, *The Physics of Amorphous Solids*, Wiley Classics Library Edition, New York **1998**.
- [52] D. Ielmini, Y. G. Zhang, *Appl. Phys. Lett.* **2007**, *90*, 192102.
- [53] N. F. Mott, *Philos. Mag.* **1969**, *19*, 835.
- [54] S. Raoux, W. Welnic, D. Ielmini, *Chem. Rev.* **2010**, *110*, 240.
- [55] J. Im, E. Cho, D. Kim, H. Horii, J. Ihm, S. Han, *Phys. Rev. B* **2010**, *81*, 245211.
- [56] P. Jost, H. Volker, A. Poitz, C. Poltorak, P. Zalden, T. Schäfer, F. R. L. Lange, R. M. Schmidt, B. Holländer, M. R. Wirtsohn, M. Wuttig, *Adv. Funct. Mater.* **2015**, DOI: 10.1002/adfm.201500848.
- [57] H. K. Mao, J. Xu, P. M. Bell, *J. Geophys. Res.* **1986**, *91*, 4673.
- [58] G. Kresse, J. Furthmüller, *Comput. Mater. Sci.* **1996**, *6*, 15.
- [59] G. Kresse, D. Joubert, *Phys. Rev. B* **1999**, *59*, 1758.
- [60] P. E. Blöchl, *Phys. Rev. B* **1994**, *50*, 17953.
- [61] T. Matsunaga, N. Yamada, Y. Kubota, *Acta Crystallogr. Sect. B-Struct. Sci.* **2004**, *60*, 685.